Joseph J, Baumann KN, Koehler P, Zuehlsdorff TJ, Cole DJ, Weber J, Bohndiek SE, Hernández-Ainsa S.

Distance dependent photoacoustics revealed through DNA nanostructures.

***Nanoscale* 2017, 9(42), 16193-16199**

Journal Name

ARTICLE

Distance dependent photoacoustics revealed through DNA nanostructures

Received 00th January 20xx,
Accepted 00th January 20xx

DOI: 10.1039/x0xx00000x

www.rsc.org/

James Joseph[a,b], Kevin N. Baumann[a], Philipp Koehler[a], Tim J. Zuehlsdorff[c], Daniel J. Cole[d], Judith Weber[a,b], Sarah E. Bohndiek[a,b*], Silvia Hernández-Ainsa[a,e,f*]

Molecular rulers that rely on the Förster resonance energy transfer (FRET) mechanism are widely used to investigate dynamic molecular processes that occur on the nanometer scale. However, the capabilities of these fluorescence molecular rulers are fundamentally limited to shallow imaging depths by light scattering in biological samples. Photoacoustic tomography (PAT) has recently emerged as a high resolution modality for in vivo imaging, coupling optical excitation with ultrasound detection. In this paper, we report the capability of PAT to probe distance-dependent FRET at centimeter depths. Using DNA nanotechnology we created several nanostructures with precisely positioned fluorophore-quencher pairs over a range of nanoscale separation distances. PAT of the DNA nanostructures showed distance-dependent photoacoustic signal enhancement and demonstrated the ability of PAT to reveal the FRET process deep within tissue mimicking phantoms. Further, we experimentally validated these DNA nanostructures as a novel and biocompatible strategy to augment the intrinsic photoacoustic signal generation capabilities of small molecule fluorescent dyes.

Introduction

Nanoscale assessment of distance-dependent fluorescence quenching has been widely utilized in nanotechnology and biomedicine to investigate dynamic molecular processes that occur on the nanometre scale.[1, 2] These fluorescence molecular rulers are fundamentally limited by light scattering in biological samples, which severely restricts the penetration depth for imaging due to the short (<100 µm) mean free path of photons in biological media.[3] As a result, the application of fluorescence-based molecular rulers is typically limited to the study of cells *in vitro*[4, 5] or to superficial applications with intravital microscopy *in vivo*.[6] Although intravital imaging based on FRET[7] mechanisms are being extensively used in various domains of cell biology[6, 8, 9] and drug discovery[8, 10, 11] they are challenged with limited penetration depth, low signal to noise ratio and photobleaching. Hence, there exists an unmet need for methodologies to probe dynamic molecular interactions that can reveal cellular responses at depth in intact living subjects.

Photoacoustic (PA) tomography is emerging as an *in vivo* preclinical imaging tool that can overcome the traditional depth limitations of all-optical imaging, providing images with a resolution of ~100 µm at depths of up to 3 cm.[12] PAT is a hybrid modality based on the absorption of pulsed light in tissue, which generates a transient thermoelastic expansion and produces an acoustic wave that can be detected by ultrasound transducers at the tissue surface. PAT requires that the decay of the optical excitation occurs via non-radiative processes to provide thermalization of the absorbed energy.[13] Fluorescence quenching is one such non-radiative decay that leads to heat dissipation into the surrounding medium.[14] We therefore hypothesized that the presence of fluorescence quenching would translate into a corresponding enhancement of the PA signal, which would therefore enable distance-dependent fluorescence quenching to be monitored at depths. Although photoacoustic imaging of small molecule dyes that can form FRET pairs in solution has been shown at supra-physiological concentrations,[15-17] precisely and mechanistically controlled distance-dependent photoacoustic behaviour has yet to be demonstrated. We achieve this here at physiologically relevant concentrations.

DNA nanotechnology is well established as a tool that enables the construction of well-defined nanostructures with a range of structural and molecular functionalities.[18, 19] Due to the accurate specificity of base-pair interactions, it is possible to obtain self-assembled DNA nanoplatforms that allow accurate positioning of various moieties with sub-nanometer precision.[20, 21] The decoration of these DNA constructs with fluorophores[22-26] has already resulted in several studies of molecular interactions based on FRET pairs using dye-dye or dye-quencher combinations. These pairs have

[a] Cavendish Laboratory, Department of Physics, University of Cambridge, Cambridge, UK
[b] Cancer Research UK Cambridge Institute, University of Cambridge, Cambridge, UK
[c] School of Natural Sciences, University of California Merced, Merced, USA
[d] School of Natural and Environmental Sciences, Newcastle University, Newcastle upon Tyne NE1 7RU, UK
[e] Present address: Instituto de Nanociencia de Aragón (INA), University of Zaragoza Campus Río Ebro, Edificio I+D, 50018 Zaragoza, Spain
[f] Present address: ARAID Foundation, University of Zaragoza, Zaragoza, Spain.
* Co-corresponding authors. Silvia Hernández-Ainsa: smh80@cam.ac.uk
Sarah E. Bohndiek: seb53@cam.ac.uk
Electronic Supplementary Information (ESI) available: [DNA nanostructures nomenclature and design, FRET calculations, Figures S1-S11 and Tables S1-S7]. See DOI: 10.1039/x0xx00000x

been used extensively in DNA nanostructures as reporters for different purposes, including molecular probes,[27] single-molecule studies,[28-31] DNA machines[32-35] and DNA walkers.[36, 37]

Here, we report a systematic study of PAT molecular rulers using DNA nanostructures to precisely tune the distance between a fluorophore and quencher pair can be potentially suitable for in vivo imaging in the near-infrared (NIR) optical window.[38] We assess the absorbance, fluorescence and photoacoustic properties of our DNA nanostructures as a function of fluorophore-quencher separation distance. Importantly, we demonstrate experimentally the potential of PAT for performing nanoscale distance measurements at depth in tissue mimicking phantoms and also highlight the utility of DNA nanostructures to enhance the photoacoustic signal generation capabilities of small molecule fluorescent dyes.

Results and discussion

In our experimental realization, we used DNA nanostructures that consist of double-stranded single helices carrying an NIR fluorophore (either IRDye 800CW or Cy5.5) and quencher (IRDye QC-1) pair at six different distances (see Figure S1 for the dye and quencher chemical structures). Selection of these particular fluorophores and quencher was made based on: their suitability for performing imaging at NIR wavelengths, aligned with the tissue optical window; their commercial availability as end modifications in DNA oligonucleotides; as well as their optimal spectral overlap for efficient fluorescence quenching. The distance between the dye and quencher was controlled by varying the number (**N**) of nucleotides (**nts**) between them (series **Nnts-DQ**, illustrated in Figure 1).

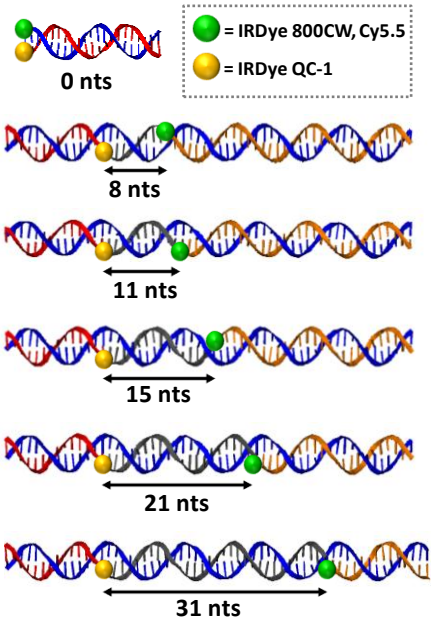

Fig.1. Schematics of the reported DNA nanostructures. Each strand contained in each of the nanostructures is represented with a different color. IRDye QC-1 quencher is represented as yellow spheres. Fluorophores (IRDye 800CW or Cy5.5) are shown as green spheres. The number of nucleotides separating the quencher and the dye on each design is represented with an arrow. The dye and the quencher are connected at the terminal part of the oligonucleotides. Series Nnts-DQ possess both the dye and quencher, series Nnts-D only dye and series Nnts-Q only the quencher. nts = Nucleotides.

We also prepared two additional series as controls (see Supporting Information section S1), carrying either the fluorophore alone (series **Nnts-D**) or the quencher alone (series **Nnts-Q**). The sequences, layout and assignment of all oligonucleotides composing the DNA nanostructures are shown in Figure S2 and Table S1. The nanostructures were prepared in phosphate buffered saline (PBS) and were analyzed with gel electrophoresis to confirm their correct folding (Figure S3).

Optical characterization of the nanostructures with N= 8 to 31nts confirmed their absorbance and distance-dependent fluorescence quenching behaviors. All characterization measurements were performed using 2 µM DNA concentration for each of the nanostructures prepared separately and were averaged over 3 replicates. The absorbance measurements for **Nnts-DQ** containing IRDye 800CW (Figure 2a) and Cy5.5 (Figure 2b) show no changes in the peak absorbance wavelengths for **Nnts-DQ** (solid-dark line) when compared to **Nnts-D** (solid-light line) and **Nnts-Q** (dotted line) nanostructures.

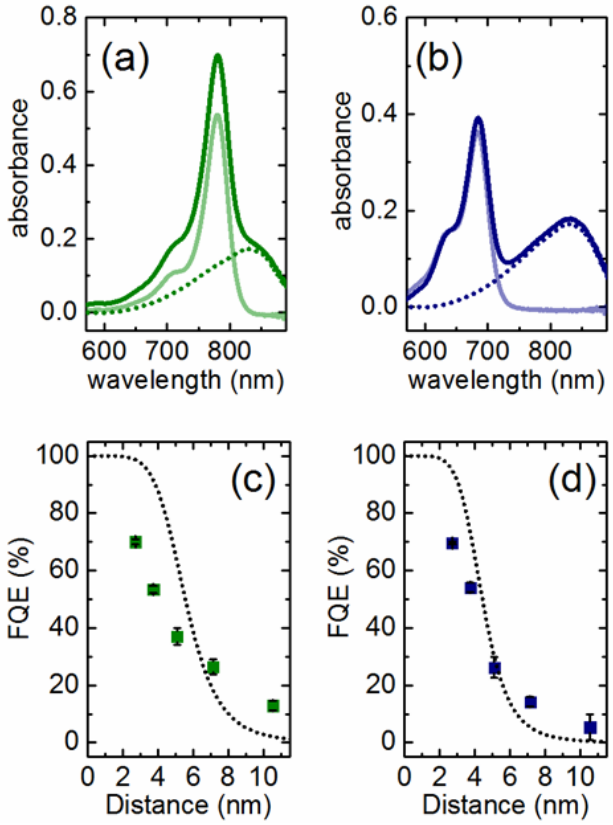

Fig.2. Optical characterization of the DNA nanostructures with spacing of N= 8, 11, 15, 21 and 31 nts. (a) and (b) Absorbance spectra of the series Nnts-DQ (solid- dark line), Nnts-D (solid- light line) and Nnts-Q (dotted line) for N=15nts derivatives (as example of the series) of (a) IRDye 800CW nanostructures and (b) Cy5.5 nanostructures. (c) and (d) Distance-dependent quenching efficiency of emission as a function of the distance between the quencher and the dye in DNA nanostructures estimated as described in Supporting Information Section S2 for (c) IRDye 800CW derivatives and (d) Cy5.5 derivatives. Quenching efficiency is calculated as described in the text. Each data point in (c) and (d) corresponds to the average of the values obtained from 3 replicates. Dotted lines represent the fitting of the experimental data to the FRET efficiency equation $E= 1/(1+(R/R_0)^6)$. Error bars indicate the error calculated as described in the Materials and Methods section-*Absorbance and emission measurements*.

Fluorescence emissions from each of the nanostructures were measured at their corresponding peak absorbance wavelengths (Table S2) to evaluate distance-dependent fluorescence quenching behavior (Figure S4). For the five different **Nnts-DQ** nanostructures, this behavior is described in terms of the fluorescence quenching efficiency (**FQE**) which is given as **(FQE= 100 x [(I_D- I_{DQ})/(I_D)])**, where I_D and I_{DQ} are the peak emission intensities obtained from the **Nnts-D** and **Nnts-DQ** nanostructures respectively. Emission measurements obtained from **Nnts-DQ** nanostructures clearly show enhanced FQE associated with corresponding shortening of the distance between the fluorophore and quencher (IRDye 800CW, Figure 2c; Cy5.5 Figure 2d). These relationships were fitted to the Förster Resonance Energy Transfer (FRET) equation, FQE= $1/(1+(R/R_0)^6$ (see dotted lines in Figure 2(c) and (d), Supporting Information section S2), indicating that the physical origin of the quenching mechanism in these nanostructures is likely to be due to FRET.

Interestingly, optical characterization of the **Nnts-DQ** nanostructures with the shortest separation (N= 0nts) showed a markedly different optical response, inconsistent with a quenching behaviour based on FRET (Figure 3 and Figure S5). The absorbance spectrum obtained from the **0nts-DQ** nanostructures carrying IRDye 800CW (full dark green line, Figure 3a) showed an additional peak at 719 nm. An equivalent blue-shifted absorbance peak (at 664 nm) was also observed in the case of the **0nts-DQ** with Cy5.5 (Figure 3b). The fluorescence emission measurements obtained from these nanostructures indicate that the FQE for the **0nts-DQ** nanostructures is extremely high for IRDye 800CW/IRDye QC-1 and Cy5.5/IRDye QC-1 (98% and 95% respectively). The observed modification of the absorbance spectra, together with the high FQE value, suggest a static quenching mechanism[39] for **0nts-DQ** nanostructures produced by the stacking of the fluorophore and quencher that is favored due to their blunt-end location.[40]

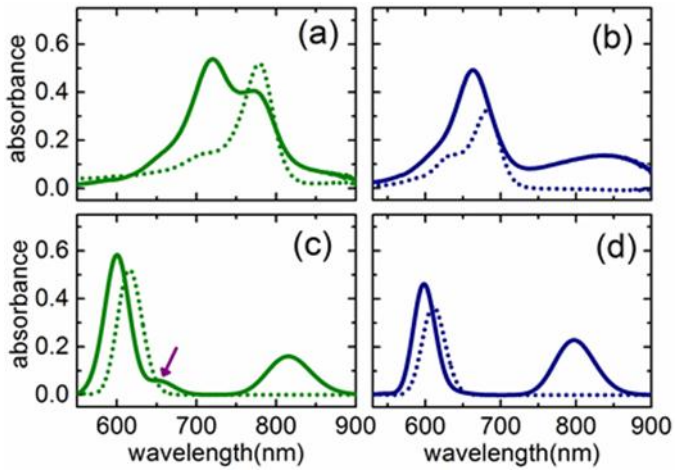

Fig.3. Optical characterization of the 0 nts DNA nanostructures. (a) and (b) Experimental absorbance spectra. (c) and (d) Theoretical absorbance spectra as predicted by TDDFT calculations. IR800CW and Cy5.5 derivatives are shown in green and blue respectively. 0nts-DQ (solid line), 0nts-D (dotted line).

In order to confirm the origin of the changes in absorbance spectra for **0nts-DQ** nanostructures, we built *in silico* model structures for **0nts-D**, **0nts-Q** and stacked fluorophore-quencher systems (**0nts-DQ**) for both IRDye 800CW/IRDye QC-1 and Cy5.5/IRDye QC-1 and computed the corresponding absorbance spectra using time-dependent density-functional theory (TDDFT) (see Materials and Methods and Supporting Information section S4 for information on the computational details and the construction of stacked fluorophore-quencher models).[41] The resultant predicted spectra in comparison with the experimental results for N= 0 nts are shown in Figure 3c and d and Figure S6. While the theoretical results overestimate the blue-shift of the main absorption peak of the fluorophore with respect to the quencher for both IRDye 800CW and Cy5.5, the spectral anomalies of **0nts-DQ** with respect to larger separations are correctly reproduced by the stacked fluorophore-quencher models.

Most notably, the TDDFT results correctly predict a blue-shift of the main absorption peak of the fluorophore, as well as a significant drop in the peak absorbance associated with IRDye QC-1. Furthermore, the theoretical results for **0nts-DQ** with IRDye 800CW also show a red-shifted second peak next to the absorbance maximum (~650 nm, see purple arrow in Figure 3c), although the peak height is lower than in the experimental results. The TDDFT results provide strong evidence to support the hypothesis that the spectral changes of **0nts-DQ** with respect to those obtained for larger separations are indeed due to a dipole coupling of the dominant excited states of the fluorophore and the quencher facilitated by a stacked conformation.[42]

We next investigated the effect of fluorescence quenching on PA signal generation under tissue mimicking conditions. Tissue mimicking phantoms provide an excellent platform to establish and validate our approach, since they enable us to perform these distance-dependent quenching measurements at 1 cm depth. Minimum detectable concentrations of small molecule contrast agents embedded in tissue mimicking phantoms, fabricated according to the same recipe used here, have previously been shown to be equivalent to those found through *in vivo* imaging in mice.[43] The DNA nanostructures were encapsulated within thin-walled plastic straws at 1 cm depth in tissue mimicking phantoms and photoacoustic images were obtained using a commercial PAT system (see Materials and Methods). Photoacoustic signals were acquired from 3 replicates of separately prepared nanostructures, using multiple excitation wavelengths and scan positions for each phantom. Quantification of the photoacoustic signals was performed by extracting the mean pixel intensity (MPI) from a region of interest (ROI) drawn within the straw position in the reconstructed images at different wavelengths (see Figure S7 and Tables S3-S5). Photoacoustic signal enhancement (PE) was then quantified as **PE= 100 x {[I_{DQ}- (I_D+I_Q)]/ (I_D+I_Q)}**, where I_{DQ}, I_D and I_Q are the averaged MPIs measured from the nanostructures of series **Nnts-DQ, Nnts-D** and **Nnts-Q** respectively. PE values were calculated from the data extracted for the wavelengths at which the absorbance for the Nnts-DQ nanostructures were maximum (Table S6).

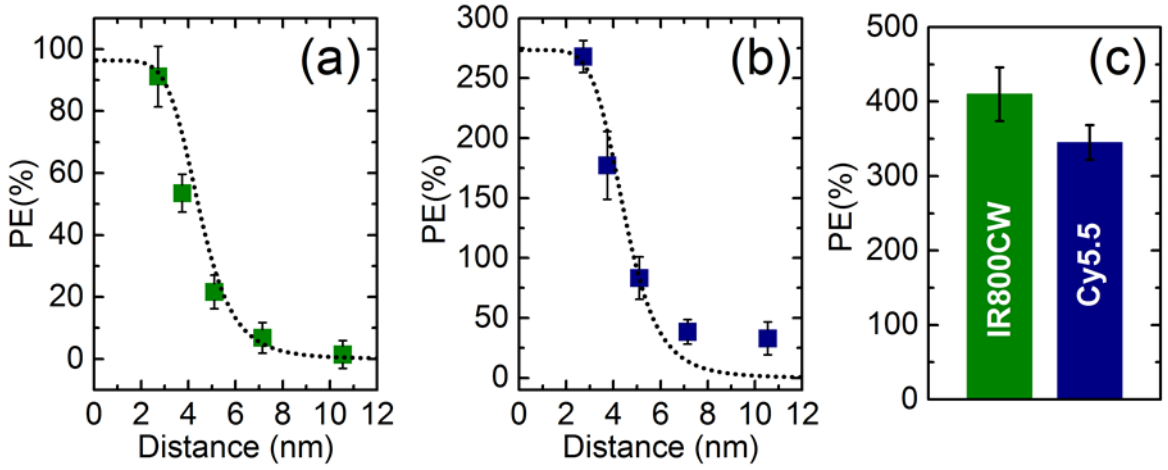

Fig.4. Photoacoustic response of the DNA nanostructures. (a) and (b) PE is given as a function of the distance between the quencher and the dye in DNA nanostructures estimated as described in Supporting Information Section S3. Dotted lines represent the fitting of the experimental data to the FRET efficiency equation $E= A*(1/(1+(R/R_0)^6))$. (c) PE obtained from the 0 nts nanostructures. Each data point in (a)-(c) corresponds to the average of the values obtained from 3 replicates. Error bars indicate the error calculated as described in the Materials and Methods section-*Photoacoustic tomography (PAT) measurements and calculations*. The reported PE values for the nanostructures with N= 8, 11, 15, 21 and 31 nts data in (a) and (b) were calculated at wavelengths of 778 nm and 682 nm for IRDye 800CW and Cy5.5 derivatives respectively. PE values for nanostructures with N= 0 nts data in (c) were calculated at 719 nm and 665 nm for IRDye 800CW and Cy5.5 derivatives respectively (see Table S6 in the Supporting Information).

The PE obtained from **Nnts-DQ** nanostructures containing IRDye 800CW (Figure 4a) and Cy5.5 (Figure 4b) show that significant enhancements in photoacoustic signal are indeed observed in a distance-dependent manner (see also Figure S7and S8). By fitting the experimental PE data to the FRET efficiency equation, given by $PE= A*(1/(1+(R/R_0)^6))$, we observed a clear dependence of PA signal on FRET behavior, as denoted by the dotted lines in Figure 4(a) and (b) (see also Supporting Information section S3). The results therefore also show a direct dependence of photoacoustic signal on fluorescence quenching, where an increased level of fluorescence quenching directly contributes to a substantial enhancement in photoacoustic signals. Of particular note are the extremely high levels of PE obtained from **0nts-DQ** nanostructures (Figure 4c) which had the shortest molecular separation and the highest fluorescence FQE. The highest level of PE occurs in the blue shifted peak identified by the absorbance measurements (Figure 3a,b and Figure S7). These results indicate with the emergence of high sensitive PAT systems that the technique could advance as imaging tool to monitor distance-dependent interactions at depth in living subjects in the future.

Conclusions

To summarize, we have shown that photoacoustic signal enhancements can be precisely tuned by controlling the distance between a fluorophore and a quencher. The mechanism of this process is related to fluorescence quenching and has been shown to occur primarily via a FRET mechanism for nanostructures N=8 to 31nts. This is the first demonstration that photoacoustic imaging can probe distance-dependent FRET behavior. Photoacoustic signal enhancement is more likely associated with static quenching at N= 0 nts due to stacking of the fluorophore and quencher molecules. The direct demonstration of the link between photoacoustic signal generation and the non-radiative decay of absorbed optical energy due to FRET suggests an exciting new approach to study the natural dynamics of key biological processes occurring at depth in intact living subjects with high resolution. In addition, the high photoacoustic signal enhancement provided by the N=0nts nanostructure could be exploited to create a biodegradable contrast agent based on small molecule fluorescent dyes as well as to promote the construction of new activatable nanoprobes for molecular imaging.[44, 45] Targeting this nanostructure to a specific biochemical process would enable highly efficient photoacoustic molecular imaging with translational potential.[38] In conclusion, we have shown that the process of fluorescence quenching can be exploited to create photoacoustic rulers, which could, in the future, be applied for studies of molecular interactions at depth in living subjects.

Materials and methods

DNA nanostructures design, assembly and characterization

The oligonucleotides were purchased from IDT (Integrated DNA Technologies, Inc). The sequences were randomly generated and NUPACK[46] was used to check that they were appropriate to minimize the formation of homodimers or hairpins. Complementary strands were obtained using the open source DNA origami software caDNAno.[47] Importantly, DNA oligonucleotides modified with the fluorophores or the quencher were stored in aliquots in the freezer wrapped in aluminium foil to prevent photobleaching of the fluorophore and quencher. The DNA strands were mixed in a stoichiometric fashion using DNA LoBind eppendorfs in phosphate buffered saline (pH=7.4) to a final concentration of 2µM DNA nanostructures (which corresponds to 2µM dye and 2µM quencher concentration). The mixture was assembled in a PCR tube by subjecting the DNA strands to thermal-annealing in a thermocycler for 45 min to ensure maximum yield in the folding. The heating program utilized was from 70 to 25°C in 90 steps (0.5°C per step, 30s each step) and the synthesized samples were stored at 4°C. Polyacrylamide gel electrophoresis (PAGE) was then performed to confirm the correct assembly. PAGE (10%) was prepared and run in a solution containing 11mM $MgCl_2$ and buffered with 0.5xTBE (pH =

8.3). 50bp DNA Ladder (Invitrogen, Thermo Fisher Scientific Inc.) was used as reference. The samples were run at 100 V for 90min. The gels were stained with GelRed for 15 minutes and visualized using a UVP gel doc-it imaging system (Figure S3).

Absorbance and emission measurements

The absorbance and fluorescence emission of the DNA nanostructures were measured at 34°C (to mimic PAT measurements temperature conditions) with a fixed concentration of 2μM of DNA. Absorbance and emission properties were measured using a UV-Vis Spectrophotometer (Varian Cary 300 Bio, Agilent Technologies, Inc.) and Fluorescence Spectrophotometer (Varian Cary Eclipse, Agilent Technologies, Inc.) respectively. Absorbance and emission data were measured at 1 nm steps. Fluorescence excitation was performed at the wavelengths detailed in Table S2, which corresponds to the respective absorbance maxima. Note that different excitation wavelengths were used for N= 8 to 31 nts and N=0 nts nanostructures due to the different maxima observed in the absorbance spectra. FQE was calculated as (FQE= 100 x $[(I_D- I_{DQ})/(I_D)]$) (Equation 1), where I_D and I_{DQ} are the peak emission intensities obtained from the Nnts-D and Nnts-DQ nanostructures respectively. The error bars in Figure 2 are the propagation of errors through Equation 1, considering the standard deviations and mean values associated to each variable (I_{DQ} and I_D). It has been well reported that the changes in the absorption spectrum of a fluorophore upon addition of a quencher provides evidence of the establishment of static quenching.[39, 40]

Time-dependent density functional theory (TDDFT) calculations

Theoretical absorbance spectra for isolated and stacked dye-quencher systems were computed using TDDFT. Well-known errors associated with standard exchange-correlation functionals, especially for excitations with intramolecular charge-transfer character, mean that absolute experimental absorption energies are not expected to be reproduced accurately.[48] However, predicted relative changes in absorption spectra can be expected to be in much closer agreement to experimental results, such that TDDFT forms a useful tool for analyzing the origin of observed changes in experimental spectra. TDDFT calculations were performed on reduced models of IRDye QC-1, IRDye 800CW and Cy5.5, while the effects of the DNA backbone were ignored (Figure S9). The initial structures of the isolated dyes were prepared using the BOSS software[49] and then reoptimized using DFT at the PBE[50] level of theory. Absorption spectra of IRDye QC-1, IRDye 800CW and Cy5.5 in isolation were calculated using an implicit solvation model with a relative dielectric constant of 80 in order to account for the screening of the aqueous environment.[51]

The two models of the stacked dye-quencher systems for a nucleotide separation of zero were obtained by taking the optimized isolated structures of IRDye QC-1, as well as IRDye 800CW and Cy5.5, and placing the dye on top of the quencher in a flat stacking, such that the alignment of the dipole moments of the dominant excitations in the individual systems is maximized. It was found that the closest stacking expected to maximize the excitonic coupling between the dye and the quencher and thus the largest changes in the absorption spectra can be achieved by rotating the quencher by 180 degrees with respect to the dye system. The initial structures for IRDye 800CW/ IRDye QC-1 and Cy5.5/IRDye QC-1 were optimized using DFT at the PBE level, where the van-der-Waals interactions between the dye and the quencher were accounted for by the empirical dispersion correction of Wu and Yang[52] (see Figure S10 for final structures of the resulting combined systems). TDDFT calculations were then performed on the two optimized, stacked dye-quencher systems, again using an implicit solvation model to account for the dielectric screening of the aqueous environment.

All DFT and TDDFT calculations were performed using the ONETEP code.[53-55] A 800 eV kinetic energy cutoff on the underlying psinc basis set and a 10 a_0 cutoff radius on all localized support functions was used throughout. All calculations were performed using the PBE functional and norm-conserving pseudopotentials. The calculation settings chosen in this work have been previously shown to yield fully converged excitation energies for small to medium sized chromophores in vacuum and solution.[41, 55]

Photoacoustic tomography (PAT) measurements and calculations

Photoacoustic measurements were performed using a commercial PAT system (inVision256-TF; iThera Medical GmbH) and tissue mimicking phantoms that closely mimic the optical and acoustic properties of biological tissues (see schematic representation in Figure S11). The commercial PAT system that has been described previously[56, 57] uses a tunable (660–1300nm) optical parametric oscillator pumped by a nanosecond pulsed Nd:YAG laser to provide 9ns excitation pulses at 10Hz repetition rate. Ten arms of a fiber bundle illuminate a ring of ~8mm width around the sample. The phantom was mounted in a motorized holder for linear translation in the z-direction over a range of <150mm. Acoustic coupling between the phantom and ultrasound transducers was achieved using a temperature maintained imaging chamber, filled with degassed, deionized water. For ultrasound detection, 256 toroidally focused ultrasound transducers specified at 5MHz center frequency, 60% bandwidth, are organized in a concave array with 270 degree angular coverage and a radius of curvature of 4 cm.

The phantoms were fabricated using agar as the base material; nigrosin dye and intralipid were added to provide an absorption coefficient of 0.05cm^{-1} and reduced scattering coefficient of 5cm^{-1} according to our standard procedure.[43] All the reagents for phantoms fabrication were purchased from Sigma Aldrich (Sigma-Aldrich Co.) unless otherwise stated. The DNA nanostructures were suspended inside sealed thin walled plastic tubes (0.3 cm diameter) that were placed at the center of the cylindrical phantoms (2 cm diameter) as shown in Figure S11b. We have shown previously that these conditions accurately mimic the optical properties of mouse tissue.[43] For all the measurements, the phantoms were maintained at 34°C inside the water bath. PAT data were acquired at the specific excitation wavelengths (see Table S3) with 10 time frames averaging and at 5 scan locations separated by a 1 mm step size for averaging over position. A model-based reconstruction algorithm[58] was used to reconstruct the PAT images and PA data were extracted at different wavelengths as shown in Table S3. Mean pixel intensity (MPI) values were extracted from a region of interest (ROI) drawn within the thin walled plastic straw and the averaged values over the 5 scan positions were used for further analysis (Tables S4 and S5). PE was quantified as PE= 100 x $\{[I_{DQ}- (I_D+I_Q)]/ (I_D+I_Q)\}$ (Equation 2) where I_{DQ}, I_D and I_Q are the averaged MPIs measured

from the nanostructures of series Nnts-DQ, Nnts-D and Nnts-Q respectively. The error bars in Figure 4 are the propagation of errors through Equation 2, considering the standard deviations and mean values associated to each variable (I_{DQ}, I_D and I_Q).

Acknowledgements

This work was funded by a Cancer Research UK Cambridge Centre Pump Prime Research Grant. JJ, JW and SEB are funded by the EPSRC-CRUK Cancer Imaging Centre in Cambridge and Manchester (C197/A16465); CRUK (C14303/A17197, C47594/A16267) and the EU-FP7-agreement FP7-PEOPLE-2013-CIG-630729. K. N. B. acknowledges the ERASMUS placement organization for ERASMUS+ funding. P. K. acknowledges funding by the EPSRC. T. J. Z. acknowledges the support of EPSRC Grant EP/J017639/1. S.H.A. acknowledges the support of a Herchel Smith postdoctoral fellowship and the ARAID foundation. The authors thank Professor U. Keyser and Mr. D. Waterhouse for valuable inputs.

References

1. E. A. Jares-Erijman and T. M. Jovin, *Nat. Biotech.*, 2003, **21**, 1387-1395.
2. J. N. Anker, W. P. Hall, O. Lyandres, N. C. Shah, J. Zhao and R. P. Van Duyne, *Nat. Mat.*, 2008, **7**, 442-453.
3. A. Taruttis and V. Ntziachristos, *Nat. Photonics*, 2015, **9**, 219-227.
4. D. W. Piston and G.-J. Kremers, *Trends Biochem. Sci.*, 2007, **32**, 407-414.
5. F. Gaits and K. Hahn, *Sci. STKE*, 2003, **2003**, pe3-pe3.
6. E. Hirata, M. R. Girotti, A. Viros, S. Hooper, B. Spencer-Dene, M. Matsuda, J. Larkin, R. Marais and E. Sahai, *Cancer Cell*, 2015, **27**, 574-588.
7. T. Förster, *Ann. Phys. (Berlin, Ger.)*, 1948, **437**, 55-75.
8. K. Aoki, Y. Kamioka and M. Matsuda, *Dev., Growth Differ.*, 2013, **55**, 515-522.
9. P. Mächler, M. T. Wyss, M. Elsayed, J. Stobart, R. Gutierrez, A. von Faber-Castell, V. Kaelin, M. Zuend, A. San Martín and I. Romero-Gómez, *Cell Metab.*, 2016, **23**, 94-102.
10. R. Bouchaala, L. Mercier, B. Andreiuk, Y. Mély, T. Vandamme, N. Anton, J. G. Goetz and A. S. Klymchenko, *J. Controlled Release*, 2016, **236**, 57-67.
11. J. Gravier, L. Sancey, S. Hirsjärvi, E. Rustique, C. Passirani, J.-P. Benoît, J.-L. Coll and I. Texier, *Mol. Pharmaceutics*, 2014, **11**, 3133-3144.
12. L. V. Wang and S. Hu, *Science*, 2012, **335**, 1458-1462.
13. L. V. Wang, *IEEE J. Sel. Top. Quantum Electron.*, 2008, **14**, 171-179.
14. R. Chance, A. Prock and R. Silbey, *Adv. Chem. Phys*, 1978, **37**, 65.
15. Y. Wang and L. V. Wang, *J. Biomed. Opt.*, 2012, **17**, 0860071-0860075.
16. Y. Wang, J. Xia and L. V. Wang, *J. Biomed. Opt.*, 2013, **18**, 101316-101316.
17. Y. Li, A. Forbrich, J. Wu, P. Shao, R. E. Campbell and R. Zemp, *Sci. Rep.*, 2016, **6**.
18. A. V. Pinheiro, D. Han, W. M. Shih and H. Yan, *Nat. Nanotechnol.*, 2011, **6**, 763-772.
19. T. J. Bandy, A. Brewer, J. R. Burns, G. Marth, T. Nguyen and E. Stulz, *Chem. Soc. Rev.*, 2011, **40**, 138-148.
20. G. P. Acuna, M. Bucher, I. H. Stein, C. Steinhauer, A. Kuzyk, P. Holzmeister, R. Schreiber, A. Moroz, F. D. Stefani and T. Liedl, *ACS Nano*, 2012, **6**, 3189-3195.
21. N. V. Voigt, T. Tørring, A. Rotaru, M. F. Jacobsen, J. B. Ravnsbæk, R. Subramani, W. Mamdouh, J. Kjems, A. Mokhir and F. Besenbacher, *Nat. Nanotechnol.*, 2010, **5**, 200-203.
22. M. Massey, W. R. Algar and U. J. Krull, *Anal. Chim. Acta*, 2006, **568**, 181-189.
23. E. A. Hemmig, C. Creatore, B. Wünsch, L. Hecker, P. Mair, M. A. Parker, S. Emmott, P. Tinnefeld, U. F. Keyser and A. W. Chin, *Nano Lett.*, 2016, **16**, 2369-2374.
24. T. Kato, H. Kashida, H. Kishida, H. Yada, H. Okamoto and H. Asanuma, *J. Am. Chem. Soc.*, 2013, **135**, 741-750.
25. S. Sindbert, S. Kalinin, H. Nguyen, A. Kienzler, L. Clima, W. Bannwarth, B. Appel, S. Müller and C. A. Seidel, *J. Am. Chem. Soc.*, 2011, **133**, 2463-2480.
26. C.-Y. Li, E. A. Hemmig, J. Kong, J. Yoo, S. Hernández-Ainsa, U. F. Keyser and A. Aksimentiev, *ACS Nano*, 2015, **9**, 1420-1433.
27. V. V. Didenko, *BioTechniques*, 2001, **31**, 1106.
28. I. H. Stein, V. Schüller, P. Böhm, P. Tinnefeld and T. Liedl, *ChemPhysChem*, 2011, **12**, 689-695.
29. R. Tsukanov, T. E. Tomov, M. Liber, Y. Berger and E. Nir, *Acc. Chem. Res.*, 2014, **47**, 1789-1798.
30. S. S. White, S. Balasubramanian, D. Klenerman and L. Ying, *Angew. Chem. Int. Ed.*, 2006, **45**, 7540-7543.
31. A. Gietl, P. Holzmeister, D. Grohmann and P. Tinnefeld, *Nucleic Acids Res.*, 2012, **40**, e110-e110.
32. P. C. Nickels, B. Wünsch, P. Holzmeister, W. Bae, L. M. Kneer, D. Grohmann, P. Tinnefeld and T. Liedl, *Science*, 2016, **354**, 305-307.
33. E. S. Andersen, M. Dong, M. M. Nielsen, K. Jahn, R. Subramani, W. Mamdouh, M. M. Golas, B. Sander, H. Stark, C. L. Oliveira, J. S. Pedersen, V. Birkedal, F. Besenbacher, K. V. Gothelf and J. Kjems, *Nature*, 2009, **459**, 73-76.
34. S. Surana, J. M. Bhat, S. P. Koushika and Y. Krishnan, *Nat. Commun.*, 2011, **2**, 340.
35. E. S. Andersen, M. Dong, M. M. Nielsen, K. Jahn, R. Subramani, W. Mamdouh, M. M. Golas, B. Sander, H. Stark and C. L. Oliveira, *Nature*, 2009, **459**, 73.
36. T. E. Tomov, R. Tsukanov, M. Liber, R. Masoud, N. Plavner and E. Nir, *J. Am. Chem. Soc.*, 2013, **135**, 11935-11941.
37. S. F. Wickham, J. Bath, Y. Katsuda, M. Endo, K. Hidaka, H. Sugiyama and A. J. Turberfield, *Nat. Nanotech.*, 2012, **7**, 169-173.
38. J. Weber, P. C. Beard and S. E. Bohndiek, *Nat. Methods*, 2016, **13**, 639-650.
39. S. A. Marras, *Methods Mol. Biol.*, 2006, 3-16.
40. S A E Marras, F R Kramer and S. Tyagi, *Nucleic Acids Res.*, 2002, **30**, 122.
41. T. J. Zuehlsdorff, P. D. Haynes, F. Hanke, M. C. Payne and N. D. Hine, *J. Chem. Theory Comput.*, 2016, **12**, 1853-1861.
42. F. Nicoli, M. K. Roos, E. A. Hemmig, M. Di Antonio, R. de Vivie-Riedle and T. Liedl, *J. Phys. Chem. A*, 2016, 9941–9947.
43. J. Joseph, M. Tomaszewski, I. Quiros-Gonzalez, J. Weber, J. Brunker and S. E. Bohndiek, *J. Nuc. Med.*, 2017, **58**, 807-814

44. Q. Miao and K. Pu, *Bioconjugate Chem.*, 2016, **27**, 2808-2823.
45. Y. Lyu, Y. Fang, Q. Miao, X. Zhen, D. Ding and K. Pu, *ACS Nano*, 2016, **10**, 4472-4481.
46. J. N. Zadeh, C. D. Steenberg, J. S. Bois, B. R. Wolfe, M. B. Pierce, A. R. Khan, R. M. Dirks and N. A. Pierce, *J. Comput. Chem.*, 2011, **32**, 170-173.
47. S. M. Douglas, A. H. Marblestone, S. Teerapittayanon, A. Vazquez, G. M. Church and W. M. Shih, *Nucleic Acids Res.*, 2009, **37**, 5001-5006.
48. N. M. Maitra, *J. Chem. Phys.* , 2016, **144**, 220901.
49. W. L. Jorgensen and J. Tirado–Rives, *J. Comp. Chem.*, 2005, **26**, 1689-1700.
50. J. P. Perdew, K. Burke and M. Ernzerhof, *Phys. Rev. Lett.*, 1996, **77**, 3865.
51. J. Dziedzic, H. H. Helal, C.-K. Skylaris, A. A. Mostofi and M. C. Payne, *Europhys. Lett.*, 2011, **95**, 43001.
52. Q. Wu and W. Yang, *J. Chem. Phys.*, 2002, **116**, 515-524.
53. T. J. Zuehlsdorff, N. D. Hine, J. S. Spencer, N. M. Harrison, D. J. Riley and P. D. Haynes, *J. Chem. Phys.*, 2013, **139**, 064104.
54. C.-K. Skylaris, P. D. Haynes, A. A. Mostofi and M. C. Payne, *J. Chem. Phys.*, 2005, **122**, 084119.
55. T. Zuehlsdorff, N. Hine, M. C. Payne and P. D. Haynes, *J. Chem. Phys.*, 2015, **143**, 204107.
56. S. Morscher, W. H. Driessen, J. Claussen and N. C. Burton, *Photoacoustics*, 2014, **2**, 103-110.
57. A. Dima, N. C. Burton and V. Ntziachristos, *J. Biomed. Opt.*, 2014, **19**, 036021-036021.
58. X. L. Dean-Ben, A. Buehler, V. Ntziachristos and D. Razansky, *IEEE Trans Med Imaging.* , 2012, **31**, 1922-1928.